INTERNATIONAL JOURNAL FOR NUMERICAL METHODS IN FLUIDS, VOL. 8, 687–704 (1988)

# FINITE ELEMENT, STREAM FUNCTION–VORTICITY SOLUTION OF SECONDARY FLOW IN THE CHANNELS OF A ROD BUNDLE

W. SLAGTER

*Netherlands Energy Research Foundation (ECN), Petten, The Netherlands*

SUMMARY

A finite element method has been applied to predict the overall features of the fully developed turbulent flow in the non-circular channels of a rod bundle. The finite element discretization is based on the conventional Galerkin method using an isoparametric quadrilateral element with mixed interpolation.

The primary axial flow and turbulent kinetic energy distributions have been predicted for fully developed turbulent flow conditions right up to the wall. The secondary velocity is represented by the stream function–vorticity formulation and the no-slip boundary conditions are explicitly introduced in the non-linear equations by a boundary vorticity formula. The Newton–Raphson method is applied to the stream function–vorticity equations and solved simultaneously by the frontal solution technique.

A one-equation eddy viscosity model of turbulence and an algebraic stress transport model have been used to predict primary axial velocity, secondary velocities and turbulent kinetic energy. The predictions obtained for a central subchannel of an equilateral-triangular rod array with $p/d = 1{\cdot}3$ are in reasonable agreement with experimental data.

## 1. INTRODUCTION

Over the past decade a number of numerical studies have been performed to predict the turbulent flow in ducts and passages of non-circular cross-section. Much of this work has been done to permit the prediction of turbulent flow and heat transfer quantities in compact passages of heat exchangers and fuel rod bundles in nuclear reactor cores. These quantities are considerably influenced by the turbulence-driven secondary flows that occur in the cross-plane of all non-circular passages. These flows cause the main flow to spiral through the passage and, although they are relatively weak compared with the main flow, they have a significant influence on the local mean flow distributions, particularly the wall shear stress and axial velocity.

Many efforts have been made to develop calculational procedures for turbulent flow in non-circular passages that include the turbulence-driven secondary flows. The relevant literature has been reviewed by Gosman and Rapley[1] and more recently by Seale.[2] The most widely used method to simulate the secondary flow has been based on simplified algebraic forms of the Reynolds stress transport equations. This algebraic stress transport model (AST model) was introduced by Launder and Ying[3] for square-duct calculations.

The primary axial flow calculations are based on a turbulence model using the eddy viscosity concept. Calculational procedures using the concept of eddy viscosity for the primary axial flow

0271–2091/88/060687–18$09.00

*Received 9 December 1986*
*Revised 19 August 1987*

together with the AST model that allows the secondary flow to be generated have been successfully applied to fully developed flow in square[3] and equilateral-triangular ducts.[4]

These procedures have also been applied to predict distributions of axial velocity, turbulent kinetic energy and secondary velocities in rod bundle geometries by a number of investigators.[1,2,5-9] In previous work[10,11] on rod bundle calculations, secondary flow was neglected and anisotropic eddy viscosities introduced to improve circumferential momentum transport.

In the present work attempts were made to predict primary axial velocity and turbulent kinetic energy as well as secondary velocities of the flow. The secondary flow is studied using the stream function-vorticity formulation. This formulation has the advantage that the pressure can be eliminated and the continuity equation is satisfied exactly. Both the axial velocity and energy of turbulence are computed directly using an one-equation eddy viscosity model of turbulence. The predictions are based on isotropic eddy viscosities and applied through the boundary layer right up to solid walls.

The inclusion of the flow region in the vicinity of walls means that solid boundary conditions can be applied exactly. It is the author's opinion that the exact application of solid boundary conditions in the computations is of prime importance to achieve convergence and correct solutions. Consequently the need for mesh refinement in the wall region for steeply varying velocity and turbulence fields has to be accepted. However, in the case of the central subchannel under consideration the wall region is relatively small in comparison with the whole area.

Another significant difference of the present work compared with that of the aforementioned investigators[1-9] is the numerical technique applied to solve the governing equations. All these researchers have used the finite difference technique in relationship with the empirical wall function formulae for specifying boundary conditions. In the present work the finite element method is applied to compute the turbulent flow quantities including the boundary layer. This numerical technique has the advantage of providing an accurate description of the complex bundle geometry, whereas regions with steep gradients can be easily refined and boundary conditions expressed in an appropriate way.

Recently, Vonka *et al.*[12] investigated secondary flow in a duct simulating an interior subchannel of a triangular array ($p/d = 1{\cdot}3$) using a laser Doppler anemometer. The results of these measurements have been compared qualitatively with the present predictions. These measurements also included other turbulent flow quantities such as primary axial velocity, turbulent kinetic energy and Reynolds stresses. However, evaluation of these measured data is still in progress.

## 2. MATHEMATICAL FORMULATION

### 2.1. *Governing equations*

The continuity equation and the fluid momentum or Navier-Stokes equations for fully developed, axial turbulent flow of a constant properties fluid in cylindrical-polar co-ordinates $(r, \phi, z)$ are

$$\frac{\partial}{r\partial r}(rV_r) + \frac{\partial V_\phi}{r\partial \phi} = 0, \tag{1}$$

*radial r-momentum*

$$V_r\frac{\partial V_r}{\partial r} + V_\phi\frac{\partial V_r}{r\partial \phi} - \frac{V_\phi^2}{r} = -\frac{1}{\rho}\frac{\partial P}{\partial r} + \nu\left(\nabla^2 V_r - \frac{V_r}{r^2} - 2\frac{\partial V_\phi}{r^2\partial \phi}\right) - \left(\frac{\partial \overline{v_r^2}}{r\partial r} + \frac{\partial \overline{v_r v_\phi}}{r\partial \phi} - \frac{\overline{v_\phi^2}}{r}\right), \tag{2}$$

*peripheral $\phi$-momentum*

$$V_r\frac{\partial V_\phi}{\partial r}+V_\phi\frac{\partial V_\phi}{r\partial\phi}+\frac{V_rV_\phi}{r}=-\frac{1}{\rho}\frac{\partial P}{r\partial\phi}+\nu\left(\nabla^2V_\phi-\frac{V_\phi}{r^2}+2\frac{\partial V_r}{r^2\partial\phi}\right)-\left(\frac{\partial\overline{v_\phi^2}}{r\partial\phi}+\frac{\partial\overline{v_rv_\phi}}{\partial r}+2\frac{\overline{v_rv_\phi}}{r}\right), \tag{3}$$

*axial z-momentum*

$$V_r\frac{\partial W}{\partial r}+V_\phi\frac{\partial W}{r\partial\phi}=-\frac{1}{\rho}\frac{\partial P}{\partial z}+\nu\nabla^2W-\left(\frac{\partial}{r\partial r}\overline{rwv_r}+\frac{\partial}{r\partial\phi}\overline{wv_\phi}\right), \tag{4}$$

where $V_r$, $V_\phi$ and $W$ are the time-averaged velocity components in the directions of the three cylindrical co-ordinates $r$, $\phi$ and $z$. The corresponding fluctuating components of the velocities are $v_r$, $v_\phi$ and $w$.

Introducing the stream function $\psi$ and axial vorticity $\omega$ as

$$\rho V_r=\partial\psi/r\partial\phi, \qquad \rho V_\phi=-\partial\psi/\partial r \tag{5}$$

and

$$\omega=\frac{1}{r}\left(\frac{\partial rV_\phi}{\partial r}-\frac{\partial V_r}{\partial\phi}\right), \tag{6}$$

the governing equations (1)–(3) yield respectively the stream function and the axial vorticity equation, i.e.

$$\frac{1}{\rho}\nabla^2\psi+\omega=0, \tag{7}$$

$$\frac{\partial}{r\partial r}\left(\omega\frac{\partial\psi}{\partial\phi}\right)-\frac{\partial}{r\partial\phi}\left(\omega\frac{\partial\psi}{\partial r}\right)-\rho\nu\nabla^2\omega+S_\omega=0, \tag{8}$$

where the vorticity production term $S_\omega$ is given by

$$S_\omega=\rho\left[\frac{\partial^2}{r\partial r\partial\phi}(\overline{v_\phi^2}-\overline{v_r^2})+\left(\frac{\partial^2}{\partial r^2}-\frac{\partial^2}{r^2\partial\phi^2}\right)\overline{v_rv_\phi}+\frac{\partial}{r^2\partial\phi}(\overline{v_\phi^2}-\overline{v_r^2})+3\frac{\partial\overline{v_rv_\phi}}{r\partial r}\right]. \tag{9}$$

This source term is written in an alternative way, i.e.

$$S_\omega=\rho\left(\frac{\partial}{r\partial r}(r\delta_r)+\frac{\partial}{r\partial\phi}(\delta_\phi)\right)=\rho\nabla\cdot\boldsymbol{\delta}, \tag{10}$$

where $\delta_r$ and $\delta_\phi$ are components of the source vector $\boldsymbol{\delta}$, defined by

$$\delta_r=\frac{\partial\overline{v_rv_\phi}}{\partial r}+2\frac{\overline{v_rv_\phi}}{r}-\frac{\partial\overline{v_r^2}}{r\partial\phi}, \qquad \delta_\phi=\frac{\partial\overline{v_\phi^2}}{\partial r}+\frac{\overline{v_\phi^2}-\overline{v_r^2}}{r}-\frac{\partial\overline{v_rv_\phi}}{r\partial\phi}. \tag{11}$$

In Section 3 it will be outlined that the modified expression for $S_\omega$ given by equations (10) and (11) is essential in the application of the finite element method.

For the axial velocity prediction the turbulence shear stresses $\overline{wv_r}$ and $\overline{wv_\phi}$ in equation (4) are defined by

$$\overline{wv_r}=-\nu_t(\partial W/\partial r), \qquad \overline{wv_\phi}=-\nu_t(\partial W/r\partial\phi), \tag{12}$$

where $\nu_t$ is the kinematic eddy viscosity of the fluid.

Substituting the eddy viscosity equation (12) into equation (4) for the axial velocity and

introducing the stream function equation (5) yields the following axial momentum equation:

$$\frac{\partial}{r\partial r}\left(W\frac{\partial\psi}{\partial\phi}\right)-\frac{\partial}{r\partial\phi}\left(W\frac{\partial\psi}{\partial r}\right)-\frac{\partial}{r\partial r}\left(r\rho(\nu+\nu_t)\frac{\partial W}{\partial r}\right)-\frac{\partial}{r\partial\phi}\left(\rho(\nu+\nu_t)\frac{\partial W}{r\partial\phi}\right)+\frac{\partial P}{\partial z}=0. \tag{13}$$

Solutions of equations (7), (8) and (13) may now be obtained for the stream function, the vorticity and the axial velocity component, providing the distribution of the eddy viscosity $\nu_t$ and the source term $S_\omega$ can be described. The turbulence quantities $\nu_t$ and $S_\omega$ will be discussed in the next subsection.

### 2.2. *Turbulence models*

In this paper a low-Reynolds-number form of the turbulence energy model proposed by Hassid and Poreh[13] is adopted to evaluate the eddy viscosity. In this model the eddy viscosity in equation (12) is related to the local values of the turbulence length scale $l$ and the turbulent kinematic energy $k$ by the Kolmogorov–Prandtl formula[14,15]

$$\nu_t=C_\nu k^{1/2}l, \tag{14}$$

where $C_\nu$ is constant.

Since the model is applied to boundary layer flows right up to the wall, the eddy viscosity is corrected for the presence of walls by introducing a damping function dependent on the turbulence Reynolds number $Rt$, i.e.

$$\nu_t=C_\nu k^{1/2}l[1-\exp(A_\nu Rt)], \tag{15}$$

where $A_\nu$ is a constant and $Rt$ is defined by

$$Rt=k^{1/2}l/\nu. \tag{16}$$

The turbulence length scale is calculated from the geometric formula suggested by Nikuradse,[16] i.e.

$$l=y[1-1{\cdot}1(y/y_0)+0{\cdot}6(y/y_0)^2-0{\cdot}15(y/y_0)^3], \tag{17}$$

where $y_0$ is the distance from the wall to the maximum velocity line along a radial line as indicated in Figure 3.

The transport equation for the turbulent kinetic energy has been derived by several authors and in the present case of fully developed axial flow the equation becomes

$$\frac{\partial}{r\partial r}\left(k\frac{\partial\psi}{\partial\phi}\right)-\frac{\partial}{r\partial\phi}\left(k\frac{\partial\psi}{\partial r}\right)-\frac{\partial}{r\partial r}\left[r\rho\left(\nu+\frac{\nu_t}{\sigma_k}\right)\frac{\partial k}{\partial r}\right]-\frac{\partial}{r\partial\phi}\left[\rho\left(\nu+\frac{\nu_t}{\sigma_k}\right)\frac{\partial k}{r\partial\phi}\right]+\varepsilon+S_k=0, \tag{18}$$

where $\varepsilon$ is the dissipation rate of turbulence energy and $S_k$ is the energy production term given by

$$S_k=-\rho\nu_t\left[\left(\frac{\partial W}{\partial r}\right)^2+\left(\frac{\partial W}{r\partial\phi}\right)^2\right]. \tag{19}$$

The turbulence model proposed by Hassid and Poreh[13] is based on the turbulence energy model introduced by Wolfshtein,[17] which has been slightly modified to give a better description of the flow features in the wall region. This modification has resulted in a simpler and physically clearer form of the dissipation term $\varepsilon$, i.e.

$$\varepsilon=2\rho(\nu+\nu_t)k/l^2. \tag{20}$$

This form satisfies the requirements that both the dissipation near the wall is balanced by the viscous diffusion and the turbulent kinetic energy at the wall is quadratic in the wall distance.

The turbulence energy model is tested by the author for fully developed turbulent pipe flow and the predictions obtained are in good agreement with experimental data for pipe flow. In this study the energy model is applied to evaluate the eddy viscosities for turbulent flow predictions in a central subchannel of a rod bundle.

It is anticipated that secondary flow plays a more dominant role in momentum transport than anisotropy and hence isotropic eddy viscosities have been assumed throughout this study. For the empirical constants the values $C_\nu = 0{\cdot}22$, $\sigma_k = 1$ and $A_\nu = 0{\cdot}012$ given by Hassid and Poreh[13] have been adopted.

The turbulence stresses in the vorticity production term $S_\omega$ are calculated from the AST model proposed by Launder and Ying:[3]

$$\overline{v_r^2} = C\frac{\nu_t}{\nu+\nu_t} l^2\left(\frac{\partial W}{\partial r}\right)^2, \qquad \overline{v_\phi^2} = C\frac{\nu_t}{\nu+\nu_t} l^2\left(\frac{\partial W}{r\partial \phi}\right)^2 \tag{21}$$

and

$$\overline{v_r v_\phi} = C\frac{\nu_t}{\nu+\nu_t} l^2\left(\frac{\partial W}{\partial r}\right)\left(\frac{\partial W}{r\partial \phi}\right), \tag{22}$$

where $C$ is a coefficient. The value of this coefficient has been varied in the computational procedure.

The term $\nu_t/(\nu+\nu_t)$ in equations (21) and (22) is additional in comparison with the original expressions introduced by Launder and Ying[3] and accounts for the near-wall turbulence being considered in the present analysis.

### 2.3. *Boundary conditions*

The final computation scheme requires solutions of the differential equations (7), (8), (13) and (18) with the auxiliary equations (15), (17), (21) and (22). Since these differential equations are all examples of quasi-linear elliptic partial differential equations, Dirichlet and Neumann boundary conditions have to be given on the whole boundary of the domain under consideration.

However, in the stream function–vorticity formulation difficulties arise with the boundary conditions for vorticity. At solid boundaries two boundary conditions are given for the stream function, called no-slip conditions, whereas no solid boundary condition exist for the vorticity. The no-slip conditions are given in the form

$$\psi = \psi_0 \qquad \textit{and} \qquad \partial\psi/\partial n = 0, \tag{23}$$

where $n$ is the outward normal.

The last condition of equation (23) will be used to obtain vorticity values on the solid boundaries. Expanding the stream function in a Taylor series around the point $\psi_0$ along the normal direction from a wall, the following relationship can be obtained:

$$\omega_0 = -\frac{2}{h^2}(\psi_1 - \psi_0), \tag{24}$$

where $h$ is the distance between the point on the wall and an interior point indicated by the subscripts 0 and 1 respectively. With specification of the boundary conditions, the statement of the stream function–vorticity problem is completed.

Furthermore, integration of the stream function equation (7) along the outward normal of a wall using the no-slip conditions of equation (23) shows that a linear variation of the vorticity at the wall results in a quadratic distribution of the stream function. This result indicates that in terms of the

finite element method the interpolation function for vorticity in the direction normal to a wall should be one degree lower than those for the stream function to satisfy the no-slip boundary conditions.

## 3. FINITE ELEMENT METHOD

### 3.1. *Method of weighted residuals*

The method of weighted residuals is employed to replace the differential equations by integral formulations. Applying the weighted residual method to obtain integral forms corresponding to equations (7) and (8), one obtains

$$\int_\Omega \Phi_1(\nabla^2\psi + \rho\omega)\mathrm{d}\Omega = 0, \tag{25}$$

$$\int_\Omega \Phi_2\left[\frac{\partial}{r\partial r}\left(\omega\frac{\partial\psi}{\partial\phi}\right) - \frac{\partial}{r\partial\phi}\left(\omega\frac{\partial\psi}{\partial r}\right) - \rho\nu\nabla^2\omega + S_\omega\right]\mathrm{d}\Omega = 0, \tag{26}$$

where $\Phi_1$ and $\Phi_2$ are weighting functions.

The value of these weighting functions is arbitrary except that they should be smooth and vanish on the part of the boundary where Dirichlet boundary conditions are specified. Since the vorticity source term $S_\omega$ is written in an alternative way by equation (10) instead of equation (9), the Gauss theorem is applicable to this term as well as to the terms $\nabla^2\psi$ and $\nabla^2\omega$ in equations (25) and (26) and gives

$$\int_\Omega (\nabla\Phi_1\cdot\nabla\psi - \Phi_1\rho\omega)\mathrm{d}\Omega = \int_\Gamma \Phi_1\frac{\partial\psi}{\partial n}\mathrm{d}\Gamma \tag{27}$$

$$\int_\Omega\left[\Phi_2\left(\frac{\partial\omega}{\partial r}\frac{\partial\psi}{r\partial\phi} - \frac{\partial\omega}{r\partial\phi}\frac{\partial\psi}{\partial r}\right) + \rho\nabla\Phi_2\cdot(\nu\nabla\omega - \boldsymbol{\delta})\right]\mathrm{d}\Omega = \int_\Gamma \rho\Phi_2\left(\nu\frac{\partial\omega}{\partial n} - \delta_n\right)\mathrm{d}\Gamma, \tag{28}$$

where $\Gamma$ is the part of the boundary where $\partial\psi/\partial n$, $\partial\omega/\partial n$ and $\delta_n$ are given. The result is that all integrands of the integrals in equations (27) and (28) contain only first-order derivatives, which is of prime importance for the finite element method. In the case of the isoparametric finite element description, however, one is forced to reduce all higher derivatives to first-order ones.

Using the Galerkin criteria to select weighting functions for the finite element formulation, the weighting function $\Phi_1$ and $\Phi_2$ are identical to the interpolation or shape functions for stream function and vorticity respectively.

### 3.2. *Finite element formulation*

In this analysis the isoparametric quadrilateral element shown in Figure 1 is employed to describe the complex rod bundle geometry.

The approximation of the axial velocity, kinetic energy and stream function over each quadrilateral element is achieved by a biquadratic interpolation function. As already stated, the interpolation function for vorticity in the direction normal to the walls has to be one degree lower than those for the stream function approximations to satisfy solid boundary requirements. This does not apply to the interpolation function in the direction parallel to the walls.

The vorticity approximation over each quadrilateral element in the co-ordinate direction parallel to the walls is treated in different ways by altering the interpolation function from

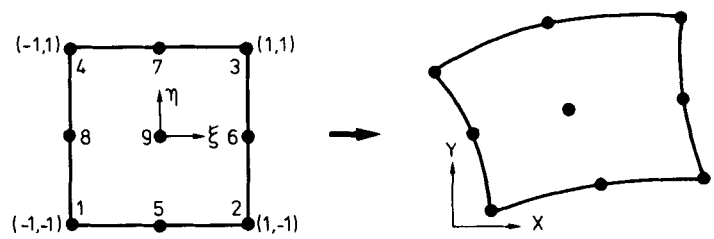


a. NON-DIMENSIONAL COORDINATES b. PHYSICAL COORDINATES

BIQUADRATIC INTERPOLATION FUNCTION FOR STREAM FUNCTION.

Figure 1. Nine-noded isoparametric quadrilateral element

quadratic to linear. A linear approximation suitable for the no-slip boundary conditions is always used in the co-ordinate direction perpendicular to the walls. The mixed interpolation formulation for the stream function–vorticity variables has already been employed by Dhatt *et al.*[18]

The resulting set of simultaneous, finite element equations in matrix form is as follows:

$$\left[\begin{array}{c|c} \mathbf{V1} & -\mathbf{K} \\ \hline \mathbf{L}\omega & +\mathbf{V2} \end{array}\right]\left\{\begin{array}{c}\psi\\ \hline \omega\end{array}\right\}=\left\{\begin{array}{c}\mathbf{R}\psi\\ \hline \mathbf{R}\omega\end{array}\right\}, \tag{29}$$

where

$$\mathbf{V1}=\int_{\Omega_e}\left[\left(\frac{\partial \mathbf{N}}{r\partial\phi}\right)^{\mathrm{T}}\frac{\partial \mathbf{N}}{r\partial\phi}+\left(\frac{\partial \mathbf{N}}{\partial r}\right)^{\mathrm{T}}\frac{\partial \mathbf{N}}{\partial r}\right]\mathrm{d}\Omega_e,$$

$$\mathbf{K}=\rho\int_{\Omega_e}\mathbf{N}^{\mathrm{T}}\mathbf{M}\mathrm{d}\Omega_e, \qquad \mathbf{R}\psi=\int_{\Gamma_e}\frac{\partial\psi}{\partial n}\mathbf{N}^{\mathrm{T}}\mathrm{d}\Gamma_e,$$

$$\mathbf{L}\omega=\int_{\Omega_e}\mathbf{M}^{\mathrm{T}}\left(\frac{\partial \mathbf{M}}{\partial r}\omega\frac{\partial \mathbf{N}}{r\partial\phi}-\frac{\partial \mathbf{M}}{r\partial\phi}\omega\frac{\partial \mathbf{N}}{\partial r}\right)\mathrm{d}\Omega_e,$$

$$\mathbf{V2}=\rho\nu\int_{\Omega_e}\left[\left(\frac{\partial \mathbf{M}}{r\partial\phi}\right)^{\mathrm{T}}\frac{\partial \mathbf{M}}{r\partial\phi}+\left(\frac{\partial \mathbf{M}}{\partial r}\right)^{\mathrm{T}}\frac{\partial \mathbf{M}}{\partial r}\right]\mathrm{d}\Omega_e,$$

$$\mathbf{R}\omega=\rho\int_{\Omega_e}\left[\delta_\phi\left(\frac{\partial \mathbf{M}}{r\partial\phi}\right)^{\mathrm{T}}+\delta_r\left(\frac{\partial \mathbf{M}}{\partial r}\right)^{\mathrm{T}}\right]\mathrm{d}\Omega_e+\rho\int_{\Gamma_e}\left(\nu\frac{\partial\omega}{\partial n}-\delta_n\right)\mathbf{M}^{\mathrm{T}}\mathrm{d}\Gamma_e.$$

In equation (29) the row vectors **N** and **M** denote the interpolation functions for $\psi$ and $\omega$, while $\psi$ and $\omega$ are column vectors with the components $\psi$ and $\omega$ as nodal values respectively.

Equation (29) is linearized by application of the Newton–Raphson method and the resulting tangent matrix **I** at element level is

$$\mathbf{I}=\left[\begin{array}{c|c} \mathbf{V1} & -\mathbf{K} \\ \hline \mathbf{L}\omega & \mathbf{V2}+\mathbf{L}\psi \end{array}\right], \tag{30}$$

where the submatrices **V1**, **V2** and **K** are constant and are identical to those in equation (29). The submatrix $\mathbf{L}\psi$ is defined as

$$\mathbf{L}\psi=\int_{\Omega_e}\mathbf{M}^{\mathrm{T}}\left(\frac{\partial \mathbf{N}}{r\partial\phi}\psi\frac{\partial \mathbf{M}}{\partial r}-\frac{\partial \mathbf{N}}{\partial r}\psi\frac{\partial \mathbf{M}}{r\partial\phi}\right)\mathrm{d}\Omega_e.$$

The terms of the non-linear submatrices $\mathbf{L}\omega$ and $\mathbf{L}\psi$ are functions of $\omega$ and $\psi$ respectively.

Assembly of the elemental equation (30) into the required global form yields equations for the whole domain under consideration. The global equations are solved within each iteration step by the frontal solution technique[19] after introducing the boundary conditions. The ordinary boundary conditions are handled in a routine manner in the finite element equations, but the stream function gradient or no-slip boundary condition at solid walls is treated by the boundary vorticity formula equation (24). This equation, which defines the nodal values of $\omega$ on the wall in terms of nodal values of $\psi$ on the wall and close to the wall, is employed to modify the assembled tangent matrix. The implementation of this equation is effected by suitable matrix manipulations.

The simultaneous solution of stream function and vorticity, together with the application of the boundary vorticity formula, results in a direct method of introducing no-slip conditions. This direct method gives fast convergent solutions for the secondary-flow problem.

The foregoing procedure, although applied to the variables of stream function and vorticity, is completely general and can also be applied to construct element matrices and vectors for axial velocity and turbulent kinetic energy. The computer program VITESSE has been developed at the author's laboratory on the above outlined principles and further details can be found in Reference 20.

## 4. NUMERICAL RESULTS AND DISCUSSION

### 4.1. *Rod bundle geometry*

The computational method is applied to analyse turbulent flow in passages of an equilateral-triangular rod array with a rod pitch/diameter ($p/d$) ratio of 1·3, as shown in Figure 2.

To study the fully developed primary flow the flow region of interest is shown in Figure 3 together with the cylindrical-polar co-ordinate system ($r$, $\phi$, $z$) used in the investigation.

The mesh is generated automatically by means of the PDA/PATRAN-G program[21] and consists of $11 \times 20$ elements with $23 \times 41$ nodes, as shown in Figure 4.

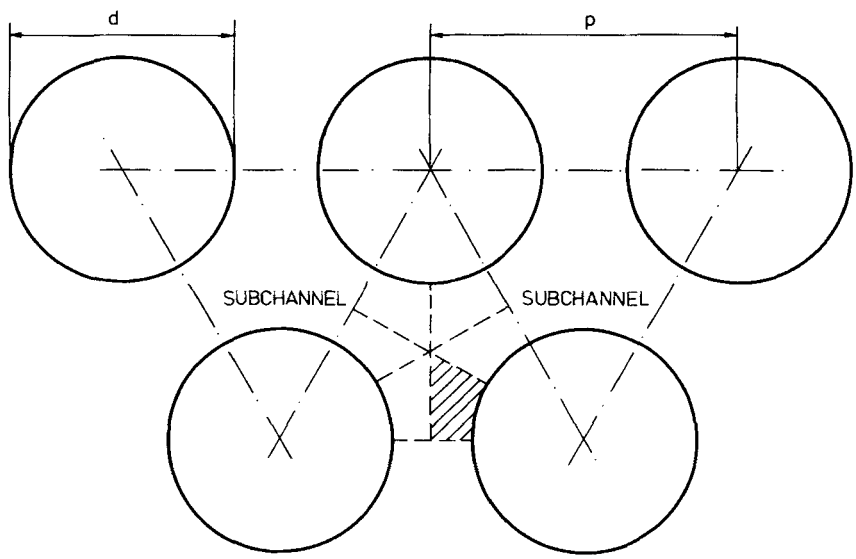


Figure 2. Cross-section of equilateral triangular rod array; the cross-hatched area represents the flow area considered

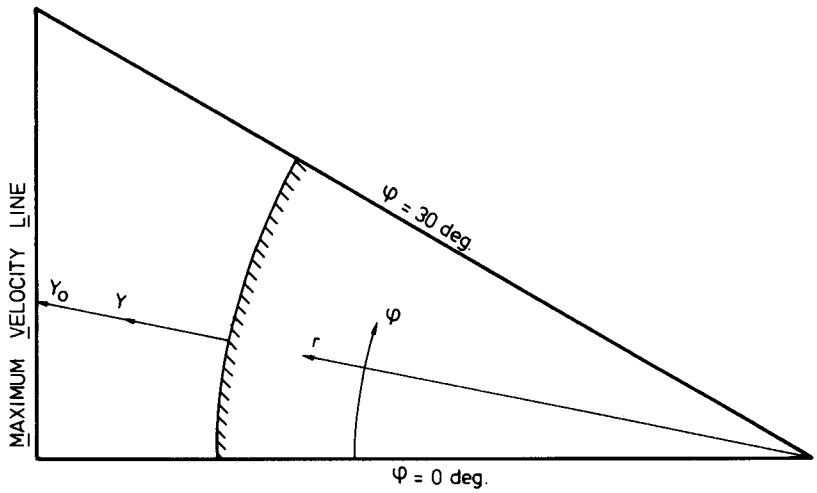


Figure 3. Cylindrical-polar co-ordinate system

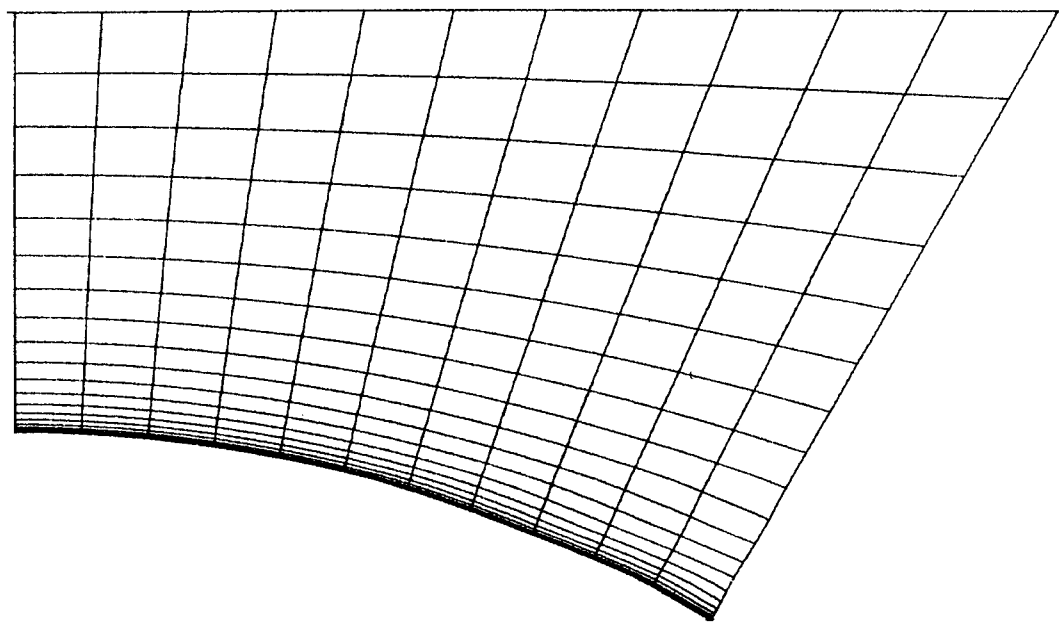

Figure 4. Finite element mesh

The isoparametric finite element representation shows that the irregular geometry of this subchannel and the required mesh refinement close to the wall are easily met by the use of this finite element formulation. The first mesh line near the wall was located at $y^+ \sim 2$ and roughly seven elements were situated within the boundary layer $y^+ \leqslant 60$.

At the solid boundary the mean axial velocity and kinetic energy are zero, whereas the normal-

to-boundary gradients of the mean axial velocity and turbulent kinetic energy were set to zero along the three non-solid boundaries as is demanded by symmetry.

The stream function is constant along all four boundaries; this constant was conveniently taken to be zero.

The vorticity is zero along the three non-solid boundaries. The unknown solid boundary condition of the vorticity is handled in a routine manner in the set of finite element equations by employing the boundary vorticity formula.

The computations were carried out for a Reynolds number $Re$ of 160000 and based on the hydraulic diameter $d_h$ of the subchannel (four times the flow area divided by the wetted perimeter).

### 4.2. *Numerical aspects*

As described in Section 3.2, two different interpolation functions for the vorticity in the circumferential direction of the rod have been applied. The results show that the linear interpolation converges much faster than the quadratic approximation. The Euclidean norm of both the stream function and the vorticity solution vectors differ by roughly one order of magnitude after ten Newton iterations. For this reason, in the remainder of this investigation the vorticity is interpolated by a linear function in both co-ordinate directions, i.e. bilinear.

Further, the numerical stability of the stream functions and the vorticity calculations was found to be quite sensitive to the coefficient $C$ in the expressions of equations (21) and (22) for the vorticity source term. The calculations were initiated with a relatively small value of $C$, say 0·0005, to ensure converged solutions.

### 4.3. *Secondary flows*

The contour plots of the vorticity in Figure 5 show a positive area adjacent to the rod separated by a zero contour from the negative-vorticity region in the central part of the channel. Positive vorticity appears also in the rectangular corner region of the symmetry lines; however, it has rather low values.

It is found that near the wall the vorticity is almost constant in the direction perpendicular to the wall.

The computed streamlines are shown in Figure 6. The location of the maximum stream function value indicates the centre of the secondary-flow vortex. The numerical results revealed at the wall a quadratic variation of the stream function with the normal wall distance. The maximum stream function value of 0·11625 was computed at the circumferential position $\phi = 17{\cdot}8°$.

Figure 7 shows the secondary-velocity vectors obtained by differentiation of the stream function with respect to the independent variables. It can be seen from this velocity vector field that the no-slip condition has been satisfied in the computation of the variables stream function and vorticity.

The maximum secondary velocities occurred near the wall in the circumferential direction and were about 0.25% of the axial bulk velocity.

The coefficient $C$ in the expressions for the components of the source term, equations (21) and (22), was set to 0·001 in deriving the computed secondary-flow results. The pattern and magnitude of the secondary flow are similar to those measured by Vonka *et al.*[12] The position of the computed secondary-flow vortex coincides roughly with the experimental vortex centre.

### 4.4. *Turbulent kinetic energy and axial velocity distributions*

A contour plot of the turbulent kinetic energy with and without secondary flow is shown in Figure 8. The effect of secondary flow is easily observed in the core of the subchannel towards the

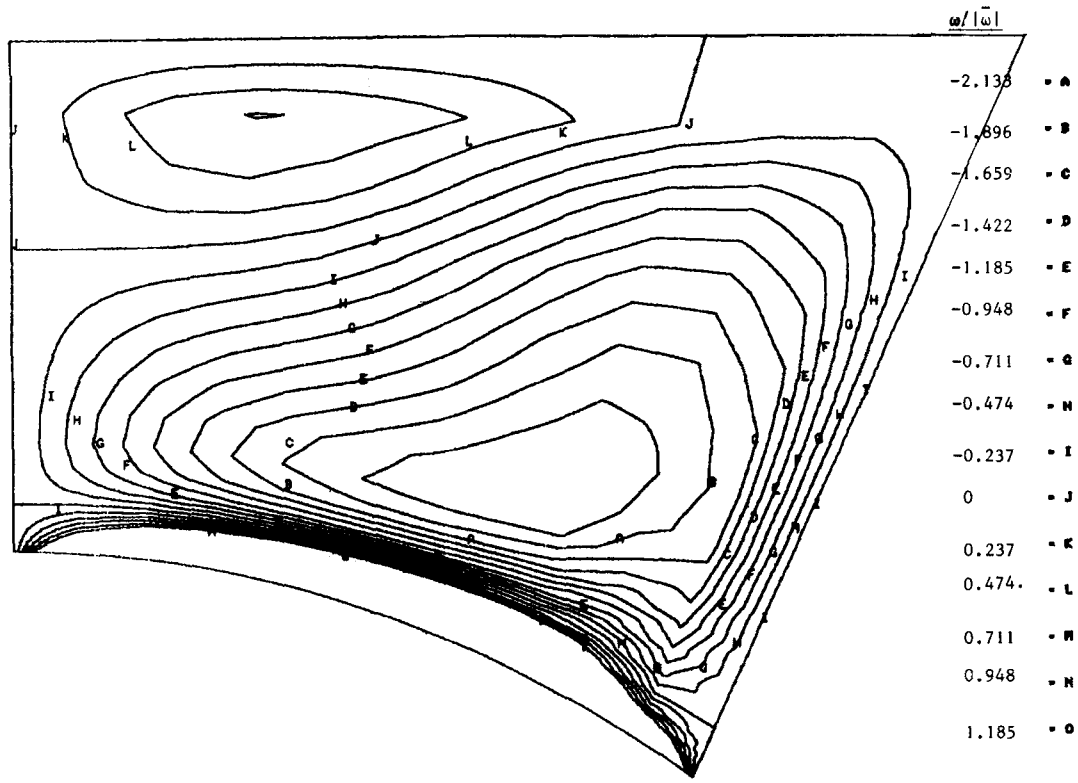


Figure 5. Equivorticity lines

symmetry line $\phi = 30°$. The computed distribution of turbulent kinetic energy is normalized with the square of the mean shear velocity.

Axial velocity contours computed with and without secondary flow are shown in Figure 9. The results revealed the influence of the secondary flow on the axial velocity distribution. In comparison with the contours predicted with secondary flow suppressed, the predicted axial velocities are more uniform—a uniformity that extends from the core region of the flow towards the rod wall.

A comparison of the numerical results with the universal velocity profiles is made in Figure 10. The predictions normalized by the local friction velocity are independent of the angular position. The good fit of the universal velocity profiles is obtained for the values of the model constants established by Hassid and Poreh.[13] For the fully turbulent part of the boundary layer, where $y^+ \geqslant 30$, close agreement is obtained between predictions and the universal law $W^+ = 2{\cdot}5 \ln y^+ + 5$ up to some maximum value of $y^+$.

The local wall shear stress is computed as $\tau_w = \rho\nu(\partial \mathbf{N}/\partial y)\mathbf{W}$, where $\mathbf{W}$ are the nodal values of the velocity at the wall and next to the wall.

The value of the computed average wall shear stress corresponds to the theoretical value. The theoretical average wall shear stress can be obtained by the balance equation for the subchannel derived from integration of the momentum equation over the channel cross-section. The wall shear

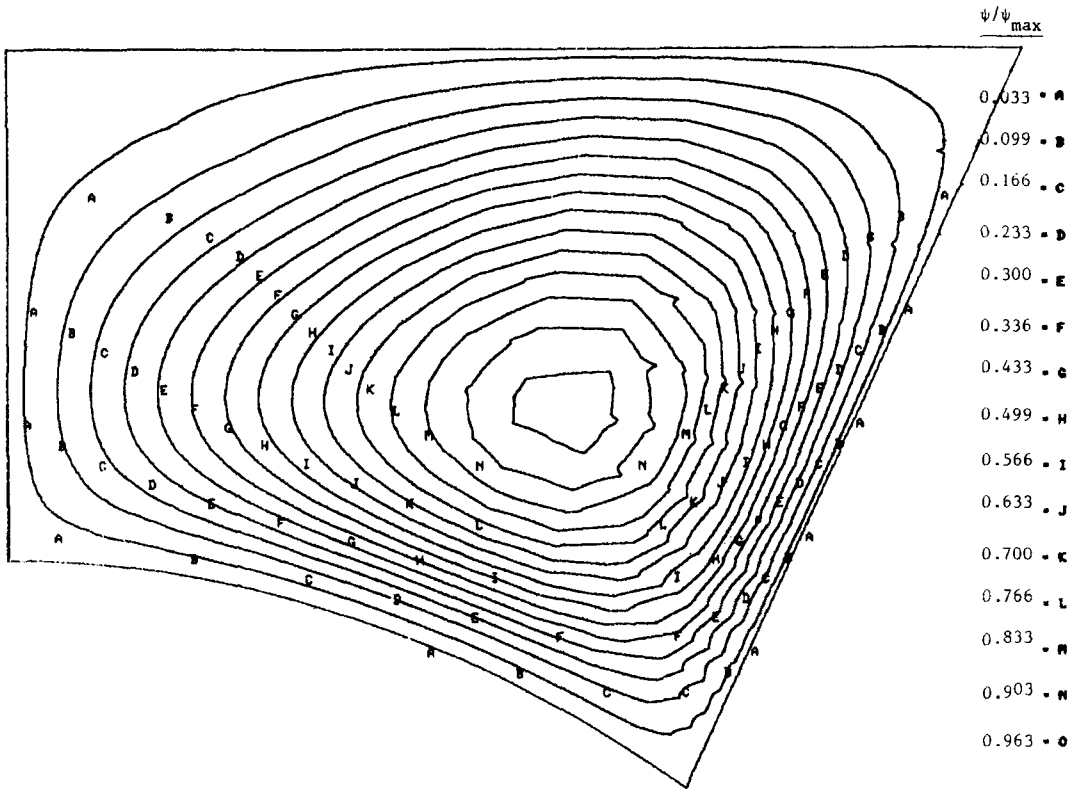


Figure 6. Streamlines

stress distribution computed both with and without secondary flows is shown in Figure 11. Suppression of the secondary flows increases the variation of the shear stress along the perimeter of the rod.

Since the pressure drop along the subchannel has to be prescribed in the computations, the friction factor was calculated as $\lambda = (\partial P/\partial z)(d_h/\frac{1}{2}\rho W_b^2)$. For the Reynolds number $Re = 160000$ used in this investigation, the value of the friction factor $\lambda$ was found to be 0·01761. This value is in close agreement with that obtained from the relationship $\lambda = 0{\cdot}19\, Re^{-0{\cdot}206}$.[2] The effect of including secondary flows in the friction factor calculations turns out to be negligibly small.

## 5. CONCLUSIONS AND REMARKS

The turbulence energy model for isotropic eddy viscosity introduced by Hassid and Poreh,[13] together with the algebraic stress transport model (AST model) proposed by Launder and Ying,[3] enabled the prediction of primary axial velocity, turbulence energy and secondary velocities. As compared with previous approaches from other investigators,[5,7] the modified form of the AST model adopted in this study can take into account secondary-flow effects up to the solid boundaries. For the particular case of fully developed flow in channels of a rod bundle with

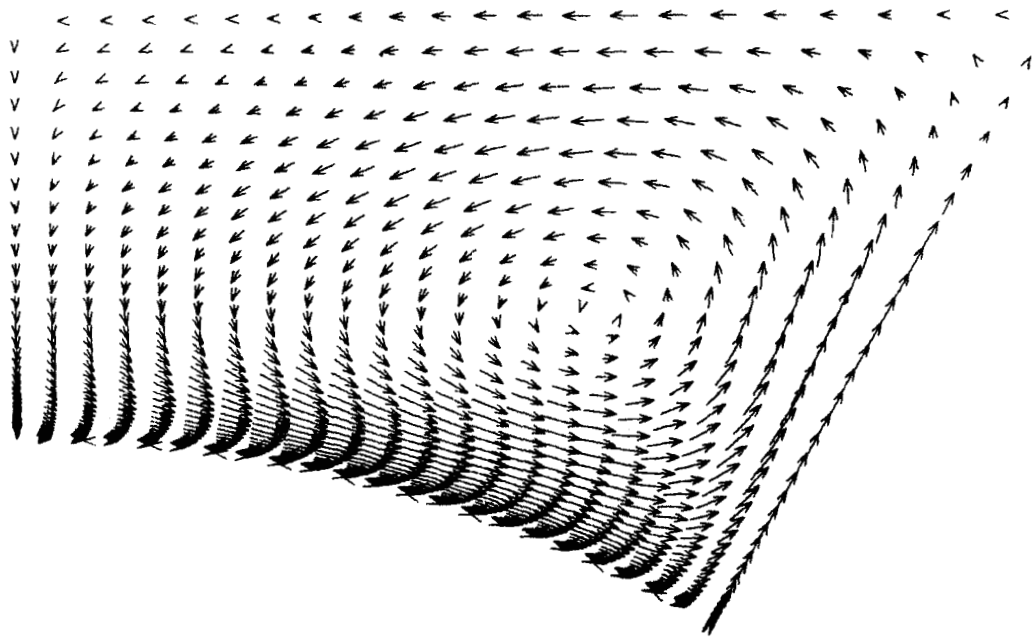

Figure 7. Secondary-velocity vector field

$p/d = 1{\cdot}3$ and $Re = 160000$, the value of coefficient $C$ in equations (21) and (22) of the AST model turns out to be 0·001.

The predicted pattern and magnitude of the secondary flow is consistent with that measured by Vonka *et al.*[12] The effect of secondary flow is evident on the primary axial flow, turbulence energy and wall shear stress distribution. It is of interest to note that the present calculation method, employing isotropic eddy viscosities and simulating secondary flow, is capable of achieving accurate detail in the prediction of local turbulent flow quantities in complex passages. The present work and results from previous work[10,11] in which secondary flow was neglected indicate that anisotropic eddy viscosities have an effect on local flow distributions similar to that of secondary flow.

The stream function–vorticity formulation for the secondary velocities has been found to work well provided that certain conditions are satisfied. First, the no-slip boundary conditions for the stream function must be applied directly, through defining vorticity boundary values by an approximate formula employed iteratively. Direct application of the boundary conditions can be achieved by the finite element discretization. Second, the order of interpolation for the vorticity must be one degree lower than those for the stream function to allow both boundary conditions to be satisfied.

The finite element method has been used for the simultaneous solution of both stream function and vorticity using Newton–Raphson iterations. It is found that the number of Newton iterations is largely influenced by the coefficient $C$ in the equations (21) and (22) of the AST model. The treatment of the vorticity source term $S_\omega$ is a novel feature in the present finite element approach of the secondary-flow analysis.

Since isoparametric elements are used, the finite element method provides an accurate description of complex bundle geometries, whereas regions with steep gradients can be easily

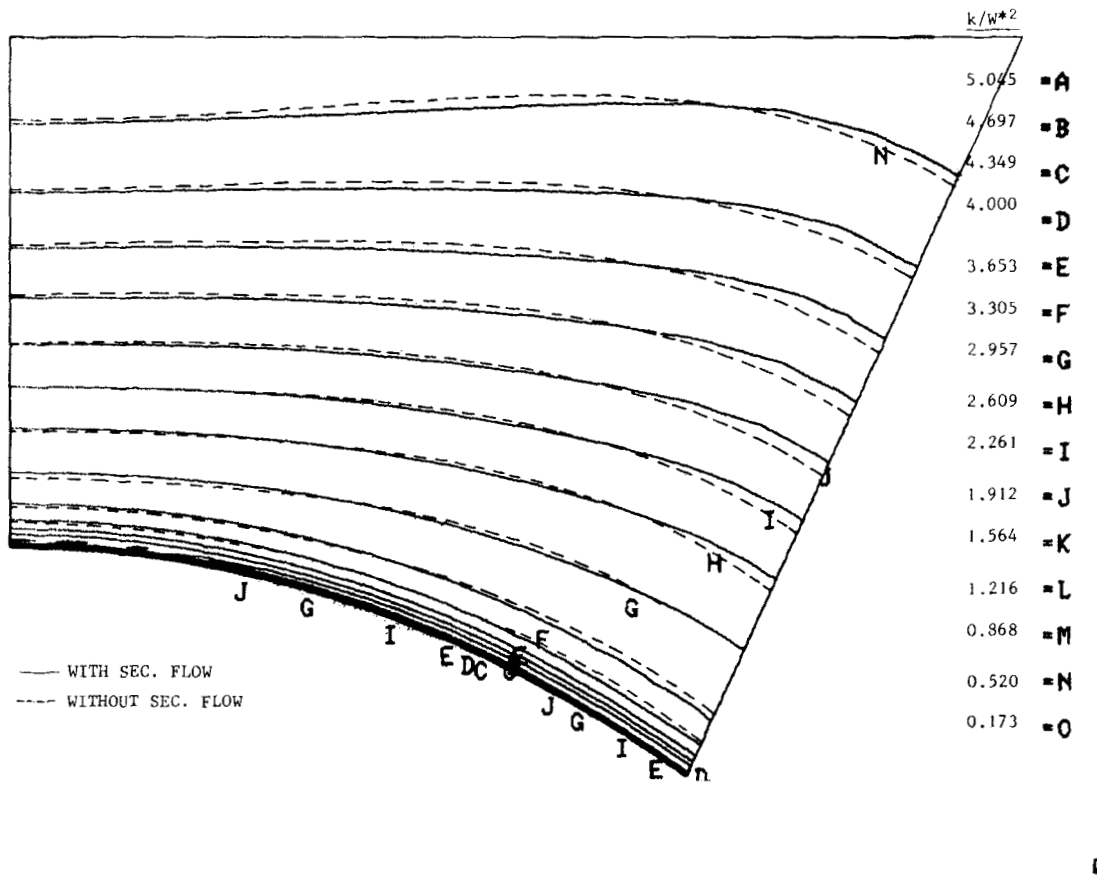


Figure 8. Contours of turbulence energy

refined and boundary conditions expressed in an appropriate way. The numerical integration is based on the Gauss–Legendre quadrature.

For secondary-flow problems the stream function–vorticity formulation has a certain measure of economy over the primitive variables approach which has been adopted by most researchers. In addition, the stream function–vorticity approach has the advantage of satisfying continuity exactly. However, the author has clear indications that increased ease in finite element computations can be achieved by treating the governing equations in terms of the primitive variables of pressure and velocity using the penalty finite element method.

The experimental work of Vonka *et al.*[12] deals with a bundle geometry of a triangular rod array and $p/d = 1{\cdot}3$. Since secondary flow is more pronounced in closely packed bundle geometries,[7] additional experimental data are necessary for code validation derived from bundle geometries with $p/d$ ratios smaller than 1·3.

From Reynolds' analogy between transport of momentum and transport of heat, as outlined by Hinze,[22] it can be deduced, in a tentative way, that, due to secondary flow, the variation in flux of heat from the rod decreases and, consequently, results in attenuation of the circumferential rod temperature differences. Since the temperature distribution within the rod bundle is of prime importance in nuclear reactor design, reliable rod temperature predictions are necessary. In this

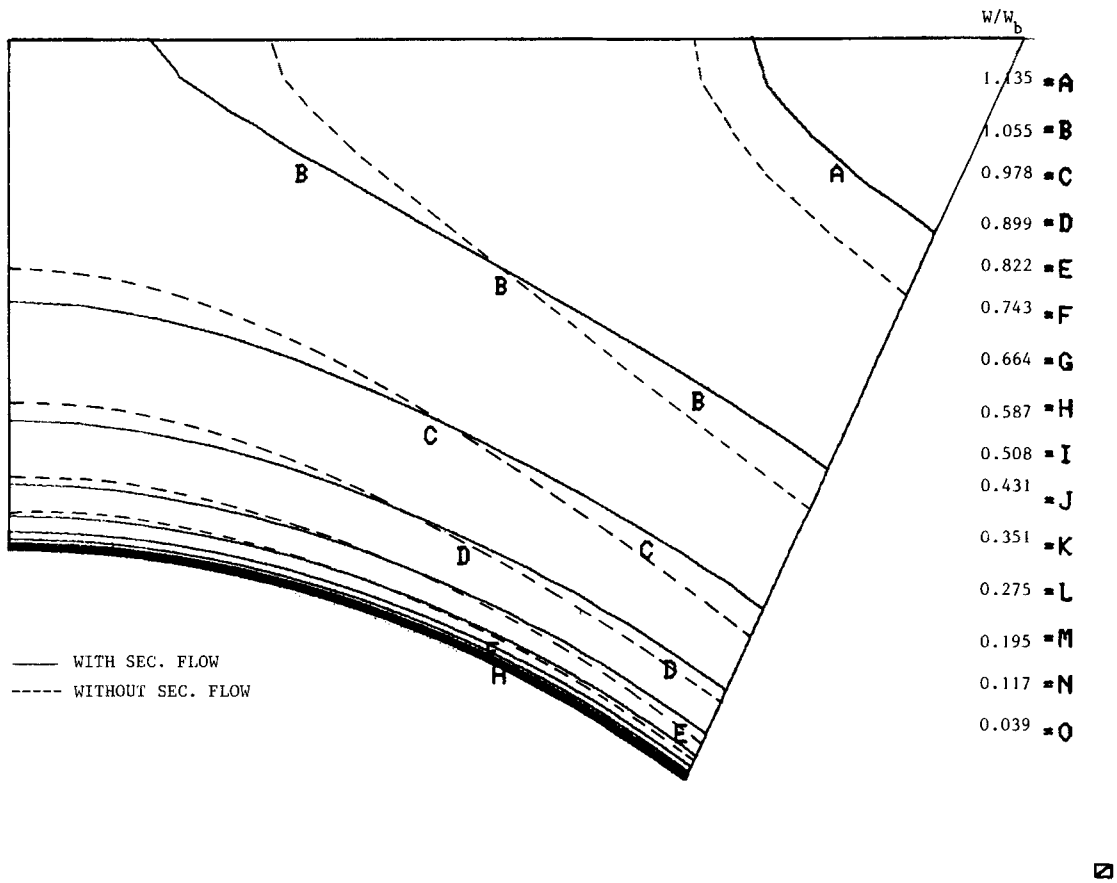


Figure 9. Contours of axial velocity

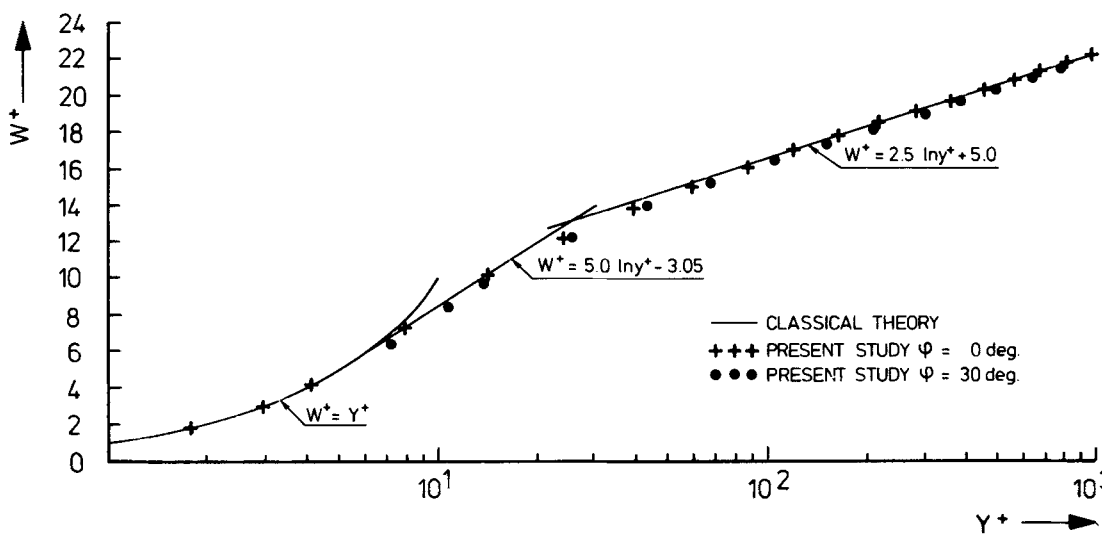


Figure 10. Dimensionless axial velocity

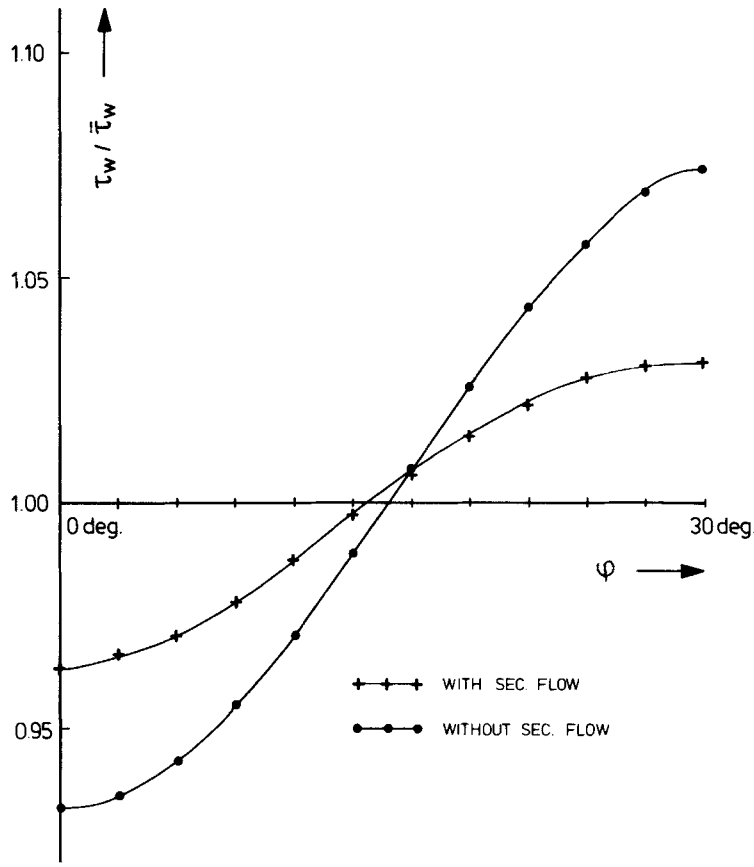


Figure 11. Wall shear stress distribution

respect the effect of secondary flow on the transport of heat in the coolant is of particular interest. However, the true role and importance of secondary flow on the transport of heat can be examined numerically. The present calculation method can provide all necessary hydraulic information to perform calculations of temperature fields in rod bundles.

ACKNOWLEDGEMENTS

The author would like to thank H. Koning and H. A. Roodbergen for their assistence and for the programming of the computer code. Thanks are also due to Debby van Huêt for her expert typing of the manuscript.

## NOMENCLATURE

| | |
|---|---|
| $A_v$ | empirical constant |
| $C$, $C_v$ | empirical constants |
| $d$ | rod diameter |
| $d_h$ | equivalent hydraulic diameter |
| $\mathbf{I}$ | tangent matrix defined by equation (30) |

| | |
|---|---|
| $k$ | turbulent kinetic energy $k=\frac{1}{2}(\bar{u}^2+\bar{v}^2+\bar{w}^2)$ |
| $k^+$ | dimensionless kinetic energy $k^+=k/W^{*2}$ |
| $\mathbf{K}$ | elemental matrix of vorticity |
| $l$ | length scale defined by equation (17) |
| $\mathbf{L}$ | elemental matrix of convective transport |
| $\mathbf{M}$ | shape function for vorticity |
| $\mathbf{n}$ | unit outward normal vector |
| $\mathbf{N}$ | shape function for axial velocity, kinetic energy and stream function |
| $p$ | pitch of rods |
| $P$ | mean static pressure |
| $r$ | radial co-ordinate |
| $\mathbf{R}$ | elemental vector |
| $Re$ | Reynolds number $Re=W_b d_h/\nu$ |
| $Rt$ | turbulence Reynolds number $Rt=lk^{1/2}/\nu$ |
| $S_k$ | source term of kinetic energy defined by equation (19) |
| $S_\omega$ | source term of vorticity defined by equation (9) |
| $v_r$, $v_\phi$, $w$ | fluctuating components of the velocities in lateral and axial directions |
| $V_r$, $V_\phi$ | time-averaged secondary velocity components |
| $\mathbf{V}$ | elemental matrix of diffusion |
| $W$ | time-averaged axial velocity component |
| $W_b$ | bulk axial velocity |
| $W^*$ | friction velocity $W^*=(\tau_w/\rho)^{1/2}$ |
| $W^+$ | dimensionless mean axial velocity $W^+=W/W^*$ |
| $z$ | axial co-ordinate |
| $y$ | radial distance from rod surface (Figure 3) |
| $y^+$ | dimensionless radial distance $y^+=yW^*/\nu$ |
| $y_0$ | radial distance from wall to MVL (maximum velocity line) (Figure 3) |

*Greek symbols*

| | |
|---|---|
| $\Gamma$ | boundary of $\Omega$ |
| $\Gamma_e$ | element boundary |
| $\boldsymbol{\delta}$ | source vector defined by equation (11) |
| $\varepsilon$ | dissipation rate of turbulent kinetic energy |
| $\eta$ | non-dimensional natural co-ordinate |
| $\lambda$ | friction factor $\lambda=(\partial P/\partial z)(d_h/\frac{1}{2}\rho W_b^2)$ |
| $\nu$ | laminar kinematic viscosity |
| $\nu_t$ | turbulent kinematic viscosity |
| $\xi$ | non-dimensional natural co-ordinate |
| $\rho$ | density |
| $\sigma_k$ | Prandtl number for turbulence energy |
| $\tau_w$ | wall shear stress $\tau_w=\rho\nu(\partial W/\partial y)_{y=0}$ |
| $\phi$ | angular co-ordinate |
| $\Phi$ | weighting function |
| $\psi$ | stream function defined by equation (5) |
| $\omega$ | axial vorticity defined by equation (6) |
| $\Omega$ | problem domain |
| $\Omega_e$ | area of an element |

## REFERENCES


1. A. D. Gosman and C. W. Rapley, 'Fully developed flow in passages of arbitrary cross section', in C. Taylor and K. Morgan (eds), *Recent Advances in Numerical Methods in Fluids*, Pineridge Press, Swansea, 1980.
2. J. Seale, 'Measurements and predictions of fully developed turbulent flow in a simulated rod bundle', *J. Fluid Mech.*, **123,** 399 (1982).
3. B. E. Launder and W. M. Ying, 'Prediction of flow and heat transfer in ducts of square cross section', *Proc. I Mech E*, **187,** 455 (1973).
4. A. M. M. Aly, A. C. Trupp and A. D. Gerrard, 'Measurement and prediction of fully developed turbulent flow in an equilateral triangular duct', *J. Fluid Mech.*, **85,** 57 (1978).
5. P. Carajilescov and N. E. Todreas, 'Experimental and analytical study of axial turbulent flows in an interior subchannel of a bare-rod bundle', *J. Heat transfer, Trans. ASME*, **98,** 262 (1976).
6. J. Seale, 'Turbulent diffusion of heat between connected flow passages, Part 2: Predictions using the $k$–$\varepsilon$ turbulence model', *Nucl. Eng. Design*, **54,** 197 (1979).
7. A. C. Trupp and A. M. M. Aly, 'Predicted turbulent flows in triangular array rod bundles', *Trans. ASME*, **101,** 354 (1979).
8. J. G. Bartzis and N. E. Todreas, 'Turbulence modeling of axial flow in a bare rod bundle', *J. Heat Transfer, Trans. ASME*, **101,** 628 (1979).
9. C. W. Rapley, 'The simulation of secondary flow effects in turbulent non-circular passage flows', *Int. j. numer. methods fluids*, **2,** 331 (1982).
10. W. Slagter, 'Finite element analysis for turbulent flows of incompressible fluids in fuel rod bundles', *Nucl. Sci. Eng.*, **66,** 84 (1978).
11. W. Slagter, 'Finite element solution of axial turbulent flow in a bare rod bundle using a one-equation turbulence model', *Nucl. Sci. Eng.*, **82,** 243 (1982).
12. V. Vonka, J. Hoornstra and P. Boersma, 'Measurements of secondary flow vortices in a rod cluster', *ECN-174*, Netherlands Energy Research Foundation, Petten, The Netherlands, 1985.
13. S. Hassid and M. Poreh, 'A turbulent energy model for flows with drag reduction', *J. Fluids Eng., Trans. ASME*, **97,** 234 (1975).
14. A. N. Kolmogorov, 'Equations of turbulent motion of an incompressible fluid', *Izv. Akad. Nauk SSSR, Ser. Phys.* **7**(1–2), 56–58 (1942).
15. L. Prandtl, 'Uber ein neues Formelsystem für die ausgebildete Turbulenz', *Nachrichten von der Akademie der Wissenshaften in Göttingen*, Van den Loeck of Ruprecht, Göttingen, 1945, pp. 6–19.
16. J. Nikuradse, 'Gesetzmässigkeiten der turbulenten Strömung in glatten Rohren', *Forschungsarbeiten Ing. Wesen*, Heft 356 (1932).
17. M. Wolfshtein, 'The velocity and temperature distribution in one-dimensional flow with turbulence augmentation and pressure gradient', *Int. J. Heat Mass Transfer*, **12,** 301 (1969).
18. G. Dhatt, B. K. Fomo and C. Bourque, 'A $\psi$–$\omega$ finite element formulation for the Navier–Stokes equations', *Int. j. numer. methods eng.*, **17,** 199 (1981).
19. P. Hood, 'Frontal solution program for unsymmetric matrices', *Int. j. numer. methods Eng.*, **10,** 379 (1976).
20. W. Slagter and H. Koning, 'Finite element, stream function–vorticity solution of secondary flow in the cross-plane of non-circular channels', *ECN-175*, Netherlands Energy Research Foundation, Petten, The Netherlands, 1985.
21. *PDA/PATRAN-G User's Manual*, PDA Engineering Software Products Division, Santa Ana.
22. J. O. Hinze, *Turbulence*, 2nd edn., McGraw-Hill, New York, 1975, p. 746.